PNAS NEXUS

PNAS Nexus, 2025, 4, pgaf118

https://doi.org/10.1093/pnasnexus/pgaf118
Advance access publication 16 April 2025
Research Report

Clear as mud redefined: Tunable transparent mineral scaffolds for visualizing microbial processes below ground

Laura K. Quinn [a,1], Kriti Sharma [b,12], Katherine T. Faber [c] and Victoria J. Orphan [b,d,*]

[a]Division of Chemistry and Chemical Engineering, California Institute of Technology, Pasadena, CA 91125, USA
[b]Division of Biology and Biological Engineering, California Institute of Technology, Pasadena, CA 91125, USA
[c]Division of Engineering and Applied Science, California Institute of Technology, Pasadena, CA 91125, USA
[d]Division of Geological and Planetary Sciences, California Institute of Technology, Pasadena, CA 91125, USA
*To whom correspondence should be addressed: Email: vorphan@caltech.edu
[1]Co-lead authors.
[2]Present address: Division of Humanities, University of California Santa Cruz.
Edited By Peter Fratzl

Abstract

Microbes inhabiting complex porous microenvironments in sediments and aquifers catalyze reactions that are critical to global biogeochemical cycles and ecosystem health. However, the opacity and complexity of porous sediment and rock matrices have considerably hindered the study of microbial processes occurring within these habitats. Here, we generated microbially compatible, optically transparent mineral scaffolds to visualize and investigate microbial colonization and activities occurring in these environments, in laboratory settings and in situ. Using inexpensive synthetic cryolite mineral, we produced optically transparent scaffolds mimicking the complex 3D structure of sediments and rocks by adapting a suspension-based, freeze-casting technique commonly used in materials science. Fine-tuning of parameters, such as freezing rate and choice of solvent, provided full control of pore size and architecture. The combined effects of scaffold porosity and structure on the movement of microbe-sized particles, tested using velocity tracking of fluorescent beads, showed diverse yet reproducible behaviors. The scaffolds we produced are compatible with epifluorescence microscopy, allowing the fluorescence-based identification of colonizing microbes by DNA-based staining and fluorescence in situ hybridization (FISH) to depths of 100 µm. Additionally, Raman spectroscopy analysis indicates minimal background signal in regions used for measuring deuterium and ^{13}C enrichment in microorganisms, highlighting the potential to directly couple D_2O or ^{13}C stable isotope probing and Raman-FISH for quantifying microbial activity at the single-cell level. To demonstrate the relevance of cryolite scaffolds for environmental field studies, we visualized their colonization by diverse microorganisms within rhizosphere sediments of a coastal seagrass plant using epifluorescence microscopy. The tool presented here enables highly resolved, spatially explicit, and multimodal investigations into the distribution, activities, and interactions of underground microbes typically obscured within opaque geological materials until now.

Keywords: soil structure, endolithic microorganisms, rock porosity, microbial colonization, spatial microbial ecology, ice templating, cryolite

Significance Statement

Porous, saturated environments, such as sediments and rocks, harbor microbes responsible for important biogeochemical cycles. However, the intrinsic opacity and complexity of such habitats make in situ investigations of these microbes extremely challenging. Here, we introduce an inexpensive, benchtop-synthesized, optically transparent, and field-deployable mineral scaffold that can be customized with specific and reproducible pore sizes and morphologies. We demonstrate that the scaffold is biocompatible and amenable to microscopy-based microbial identity and activity measurements. The ability to visualize and characterize colonizing microbes within transparent surrogates of opaque environments constitutes an important advance in environmental microbiology, providing a model for studying microbial processes occurring in habitats including sediments, saturated soils, and permeable aquifer rock. This versatile tool will undoubtedly boost our mechanistic understanding of microbial processes belowground.

Competing Interest: The authors declare no competing interests.
Received: October 5, 2024. **Accepted:** March 31, 2025

Introduction

Natural ecosystems, such as sediments, aquifers, saturated soils and rocks, harbor thousands of co-occurring and interacting microbial species that are crucial for global geochemical cycling and that may be harnessed for key chemical transformations, including the oxidation of the greenhouse gas methane, and the remediation of heavy metals from wastewater (1–3). Ubiquitous habitats like these are porous and opaque, physically and chemically complex, temporally dynamic, and spatially heterogeneous (4–6). Such features represent enormous limitations for our understanding of the microbial processes occurring in these environments. Specifically, these limitations have hindered our ability to (i) visualize belowground microorganisms, (ii) characterize their interactions, and (iii) quantify microbial activities at a fine scale in situ. To gain a comprehensive understanding of the dynamics driving these microbial communities and their activities, nondestructive, real-time imaging within complex porous materials is essential.

An ideal experimental soil or rock system for microbial observation and analysis should be transparent in aqueous media, nontoxic to bacteria, and able to support a variety of pore structures to mimic the diverse pore morphologies characteristic of natural sediment and aquifer microenvironments. Pioneering microbiologists in the 1930s introduced the use of microscope slides deployed in the environment (i.e. the Cholodny and Rossi technique) to great success in the study of microbial colonization of surfaces (7, 8); however, slides do not capture the inherent pore structure complexity in situ. More recent advancements with structured devices (including micro- and meso-fluidic platforms) have been built to simulate certain physical properties of porous environments while being transparent and manipulable and thus amenable to fine-tuning and direct observation (9–13). While adding complexity, these devices do not reproduce the 3D structure of porous habitats but rather reduce it to 2Ds, to ensure tractability. Moreover, such microfluidic devices are rarely field deployable. Microbes are generally cultured or removed from the natural environment and subsequently *loaded* in a controlled way into the device containing a medium. One of the few devices allowing in situ microbial cultivation is the iChip, where researchers were able to grow microorganisms taken from soil, load them into the device's chambers, and deploy them back within the soil environment (14). However, despite its field capabilities, the iChip is not transparent, does not allow for natural colonization, and lacks features enabling the characterization of microbial interactions and activities.

Another promising candidate for fabricating porous yet manipulable and observable scaffolds is "transparent soil" (TS)—particulate materials that can be engineered to be optically transparent. The technique to create TSs was first used to study interactions between soil and structure and the effects of saturation on hydraulic behavior (for example, (15)), but TSs have since emerged as promising candidates for use as a simulated bacterial habitat for microscopic observation. Research into TSs for supporting bacterial or plant life has utilized many different materials, including hydrogels, Nafion, and silica (SiO_2) (16–23). However, most TS studies have used loosely packed materials, whose structure can be difficult to control and replicate, and that does not enable customizable pore morphologies. Moreover, as loose materials, TSs are not generally amenable to field deployment and retrieval.

More recently, Sharma et al. (17) established natural cryolite (Na_3AlF_6) as a promising TS scaffold. Cryolite has a refractive index (RI) of 1.34, very close to that of water (24) and is, therefore, transparent in aqueous media. Sharma et al. (17) showed that ground natural cryolite crystals were compatible with several biologically relevant imaging techniques, including fluorescence microscopy, as well as single-cell Raman spectroscopy, an analytical method used in combination with D-labeled water or ^{13}C-carbon substrates to track microbial activity. While naturally occurring cryolite mineral has been mined almost to extinction (25, 26), synthetic cryolite powder is inexpensive and abundantly available through scientific and commercial suppliers. So far, however, its utility as a transparent model of geological matrices for studying microbial colonization and activity has not been tested.

Here, we introduce tunable, deployable, and transparent synthetic cryolite scaffolds that mimic the porous structure of sediments and rocks. To create them, we employed a commonly used method in materials science known as freeze casting. This facile and versatile technique has been used to create porous metals (27), glasses (28), polymers (29, 30), and ceramics (31–33). Freeze casting is compatible with multiple materials and solvents to produce a range of pore morphologies and chemical compositions tailored to the intended application in physics, chemistry, environmental sciences, and biomedicine (32, 34–38). The microbially compatible scaffolds produced here provide realistic and complex 3D habitats for microbes, and microbial interactions, and processes can be characterized and quantified after retrieval, using light microscopy (fluorescence and brightfield) and Raman spectroscopy. This new tool was successfully deployed within coastal seagrass rhizosphere sediment to investigate the in situ colonization patterns of native environmental microbes.

Results and discussion

Cryolite freeze casting and chemical characterization

Synthetic cryolite powder is inexpensive and widely available, but unlike powdered natural cryolite crystals, it is not transparent on its own. To create a transparent scaffold, the synthetic powder was first freeze cast to incorporate pore structure into a scaffold, followed by sintering to create a robust, transparent material. In this suspension-based freeze-casting process, synthetic cryolite powder was first suspended in a solvent with the aid of a dispersant that ensured the cryolite remained suspended until freezing began (see Materials and methods). The suspension was pipetted into a Pyrex mold on the freeze-casting setup, and the temperature of the cold plate was lowered to initiate directional freezing of the solvent (Fig. 1a (39)). As solvent crystals grow, they push aside the suspended cryolite to create a biphasic material of cryolite and solvent crystals. The crystals were subsequently removed through sublimation, leaving behind negative impressions forming the pore network in the cryolite. The resulting porous cryolite scaffold was then heat treated to create a hardened structure that was transparent when saturated with water. This transparency was unique to cryolite and not observed with similar freeze-cast scaffolds using silicon oxycarbide (SiOC) and silica (SiO_2; Fig. 1b). However, when dry, the cryolite was also opaque. This indicates that RI matching was a key source of the scaffolds' transparency.

Several variables in the freeze-casting process can be altered to produce a variety of pore morphologies (Fig. 1c (40)). For example, using cyclohexane or cyclooctane as the freezing solvent produced dendritic and isotropic pore networks, respectively, while changing the freezing rate of a cyclohexane system produced columnar pores here demonstrated using a conventional preceramic polymer-derived SiOC matrix. Dendritic pores are characterized

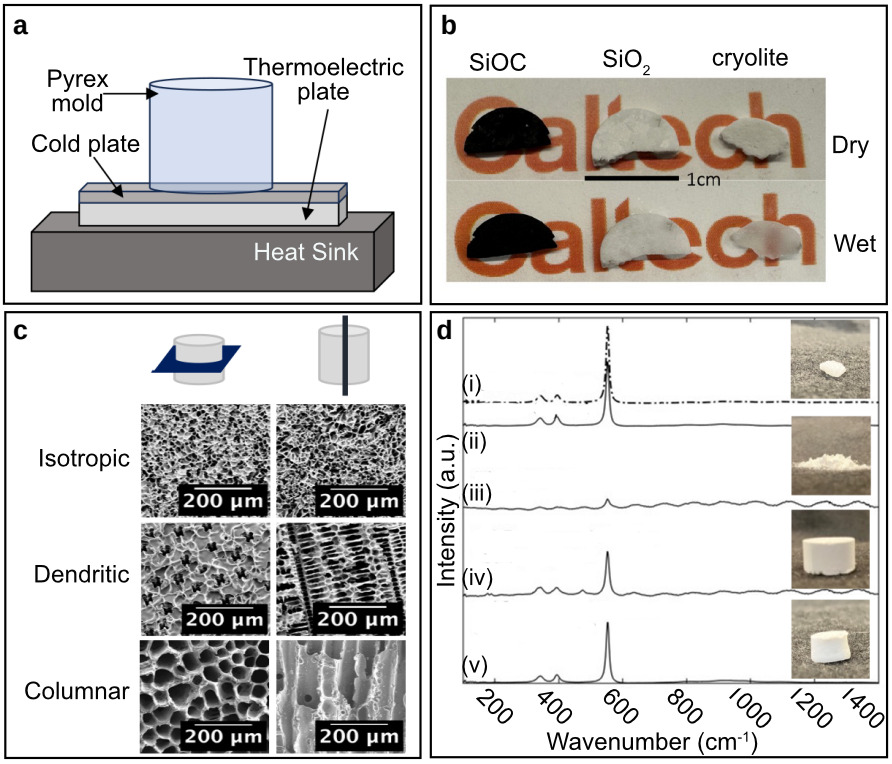

Fig. 1. a) Schematic of the single-sided freeze-casting setup in which solvent crystals grow directionally from the cold plate upwards. b) Dry and water-saturated SiOC, SiO_2, and freeze-cast synthetic cryolite (Na_3AlF_6) scaffolds, each cut to a thickness of ~2 mm, illustrate the difference in transparency between the water-saturated cryolite and other freeze cast dendritic porous structures of comparable thicknesses. c) An example of the potential to customize distinct pore morphologies and structures using freeze-casting techniques is illustrated with SiOC showing transverse and longitudinal cross-sections of dendritic, isotropic, and columnar scaffolds. Similar structures were achieved using synthetic cryolite (see Fig. 2). d) Raman spectra of (i) ground (dashed line) and (ii) whole natural cryolite crystal (solid line), (iii) off-the-shelf synthetic cryolite powder, and synthetic cryolite powder after freeze casting with (iv) 600 °C in air, and (v) 900 °C under argon gas. Inset images show the natural and synthetic cryolite materials corresponding with the Raman spectra.

by primary pores that are highly aligned with the freezing direction, with secondary pores branching off from the primary pores. Conversely, in sponge-like, isotropic pore networks, the pores appear similar, whether cross-sectioned parallel or perpendicular to the freezing direction. Finally, columnar pores are also highly aligned with the freezing direction but lack any secondary branching pore and instead produce a honeycomb-like pore network. Similar structures were generated with freeze-casting synthetic cryolite (described below).

The synthetic cryolite powder processed for freeze casting was chemically identical to natural cryolite crystals. We tested the chemical composition and crystallinity of the synthetic cryolite at various stages throughout the freeze-casting process using Raman spectroscopy. Our data showed that whole crystals and powders of natural cryolite both exhibit a clear Raman spectrum with a strong peak around 550 cm^{-1} and two weaker peaks around 350 and 400 cm^{-1} (Fig. 1d). This was notably distinct from the off-the-shelf synthetic cryolite powder, which exhibited only a very weak Raman spectral peak at 550 cm^{-1} and had a sinusoidal background attributed to optical interference in the spectrometer. To produce a better-ordered lattice, like that of the naturally occurring cryolite crystals, we heat treated the synthetic cryolite with temperatures corresponding to the sintering temperatures used in the freeze-casting process (see Materials and methods). Analysis by Raman spectroscopy confirmed that these additional sintering steps of the synthetic cryolite did not significantly change the chemical composition of the freeze-cast structure, producing a spectrum nearly identical to that of the natural cryolite crystal (Fig. 1d). Through these heat-treating steps, synthetic cryolite powder can be transformed into an ordered lattice resembling naturally occurring cryolite with similar optical properties, without altering the material's chemical composition.

Pore morphology characterization

Pore morphology is an important parameter in the context of below-ground microbiological processes, as it influences nutrient flow, waste removal, and, presumably, the distribution and type of cells colonizing and growing within the scaffolds. Freeze casting enables customization of various pore sizes and morphologies through choice of solvent, solids loading, or freezing rate (Table 1). We synthesized cryolite scaffolds with four different pore structures (12 and 24 vol.% dendritic, 12 vol.% columnar, and 12 vol.% isotropic pores; Figs. 2 and S1). The dendritic and columnar pore morphologies had pores oriented along the axis of the freezing direction, while isotropic pore morphologies exhibited a nondirectional, sponge-like pore network. Mercury intrusion porosimetry was used to quantify pore size distributions. The 12 vol.% dendritic pore morphology (used for microbial experiments described later in this work) had a bimodal pore size distribution, with primary channel pores having a width of ~25 µm, with secondary arms around 20 µm. These pore sizes are large enough to accommodate single cells, small microbial aggregates, or biofilms. Scanning electron microscopy (SEM) imaging of the dendritic scaffold shows pores both perpendicular to and parallel with the freezing direction (Fig. 2a). In the longitudinal SEM image, primary dendrite channels parallel to the freezing direction can

Table 1. Freeze casting and sintering parameters for cryolite samples.

Sample name	Vol.% cryolite	Solvent	Wt.% dispersant	Freeze-casting setup	Freezing rate (mm/s)
Dendritic 12 vol.%	12	Cyclohexane	4	Single sided	15
Dendritic 24 vol.%	24	Cyclohexane	4	Single sided	15
Isotropic 12 vol.%	12	Cyclooctane	4	Single sided	15
Columnar 12 vol.%	12	Cyclohexane	10	Double sided	1

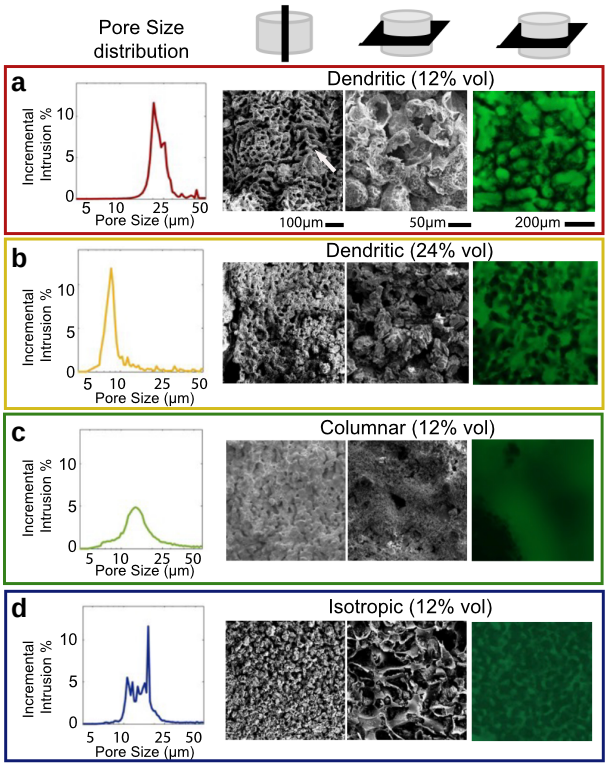

Fig. 2. Pore size distributions of different freeze-cast synthetic cryolite scaffolds measured by mercury intrusion porosimetry (first column) and visualized in SEM images. Longitudinal (second column) and transverse (third column) cuts are shown for a) 12 vol.% dendritic, b) 24 vol.% dendritic, c) 12 vol.% columnar, and d) 12 vol.% isotropic scaffolds. The white arrow on the image of the 12 vol.% dendritic scaffold points to the pore wall of the primary pore channel, with darker secondary pores branching off from it. The fourth column shows the saturated pore space (in green) dyed with a fluorescein solution for the four different pore morphologies imaged by confocal microscopy at 500–550 nm. Images of additional fluorescence channels are provided in Fig. S1.

be seen with slightly smaller secondary dendrite arms branching off from the primary channel. These two different size regimes of pores enable colonization of the smaller, secondary dendrite pores with lower flow rates, while higher flow across the larger primary dendrite channels can enhance nutrient delivery or metabolic waste removal (41, 42).

Increasing the cryolite solids loading to 24 vol.% in the initial freeze-casting suspension resulted in smaller pore sizes. As seen in Fig. 2b, the pore size distribution shifted to smaller pores with less bimodal character (primary dendrite arms ~11 μm and secondary arms of order 8 μm), compared with the 12 vol.% cryolite dendritic scaffold (primary dendrite arms ~25 μm and secondary dendrite arms ~20 μm). This was also independently observed in the SEM images (Fig. 2b). Both 12 and 24 vol.% scaffolds were frozen under the same conditions, confirming that altering the solids loading of synthetic cryolite in the freeze-casting process can be used to control pore size, an important variable alongside pore morphology for studying bacterial processes in rocks and saturated soils.

To produce the columnar morphology, the cryolite suspension was frozen at a slower rate than the dendritic scaffolds, producing a unimodal pore size distribution (~15 μm on average; Fig. 2c). While the pores of the columnar scaffolds are large enough to allow for microbial colonization, they lack side channels for bacteria to colonize off the main channel, predicted to generate different flow and particle transport patterns within the scaffold (Fig. 2c).

High-tortuosity (isotropic) morphologies were also synthesized using freeze casting by using cyclooctane instead of cyclohexane in the freeze-casting suspension (see Materials and methods). The pore size distribution of the isotropic morphology was highly variable, between ~10 and 25 μm. SEM images confirmed the heterogeneity of pore sizes and revealed that the isotropic pore morphology was similar in both the transverse and longitudinal directions (Fig. 2d).

The pore morphologies were also visualized using fluorescence confocal microscopy, providing a nondestructive means of tracking the physical scaffold characteristics. The confocal images in Fig. 2 show the four scaffold morphologies after saturation with a fluorescein solution in nanopure water. The fluorescein-filled pore spaces are visible in the green fluorescence channel (fluorescein isothiocyanate [FITC]), highlighting the distinct boundaries between the sintered cryolite and the pore spaces. Confocal imaging of these porous cryolite samples additionally demonstrated that water fully permeated the scaffold. Together, these four morphologies offer a wide range of customizable pore sizes and shapes for microbial and geochemical investigations through tuning of the freezing rate, solvent, or solids loading during cryolite freeze casting.

Transparency assessments

A key aspect determining the utility of transparent scaffolds for microbial investigations is the depth of light penetration and resolution. The visibility of beads in dendritic SiOC, SiO_2, and cryolite (Na_3AlF_6) scaffolds was compared using confocal microscopy by imaging fluorescent beads (1 μm diameter) in pore spaces adjacent to the coverslip and at a depth of 20 μm (depth for comparison was selected based on the depth where the signal was no longer visible in SiOC; Fig. 3a). Fluorescent beads could not be detected at depths >20 μm in the dendritic SiOC and were only visible in SiO_2 at depths >20 μm when imaging within an open-pore channel that was well aligned with the imaging axis (i.e. unobstructed by the SiO_2 scaffold material). Conversely, in the dendritic, water-saturated cryolite scaffold, RI matching enabled clear visualization of fluorescent beads at depths of at least 20 μm from the sample surface, regardless of their location within the scaffold. Routine detection was possible at 75 μm and up to 100 μm, as discussed below (Fig. 3b).

To test the maximal depth of resolution for microbe-sized particles, the maximum intensity of 1 μm fluorescent beads was measured as a function of depth within each porous scaffold comprised of different materials and pore structures (Fig. 3b). Beads within a dendritic SiOC scaffold, which is opaque even when

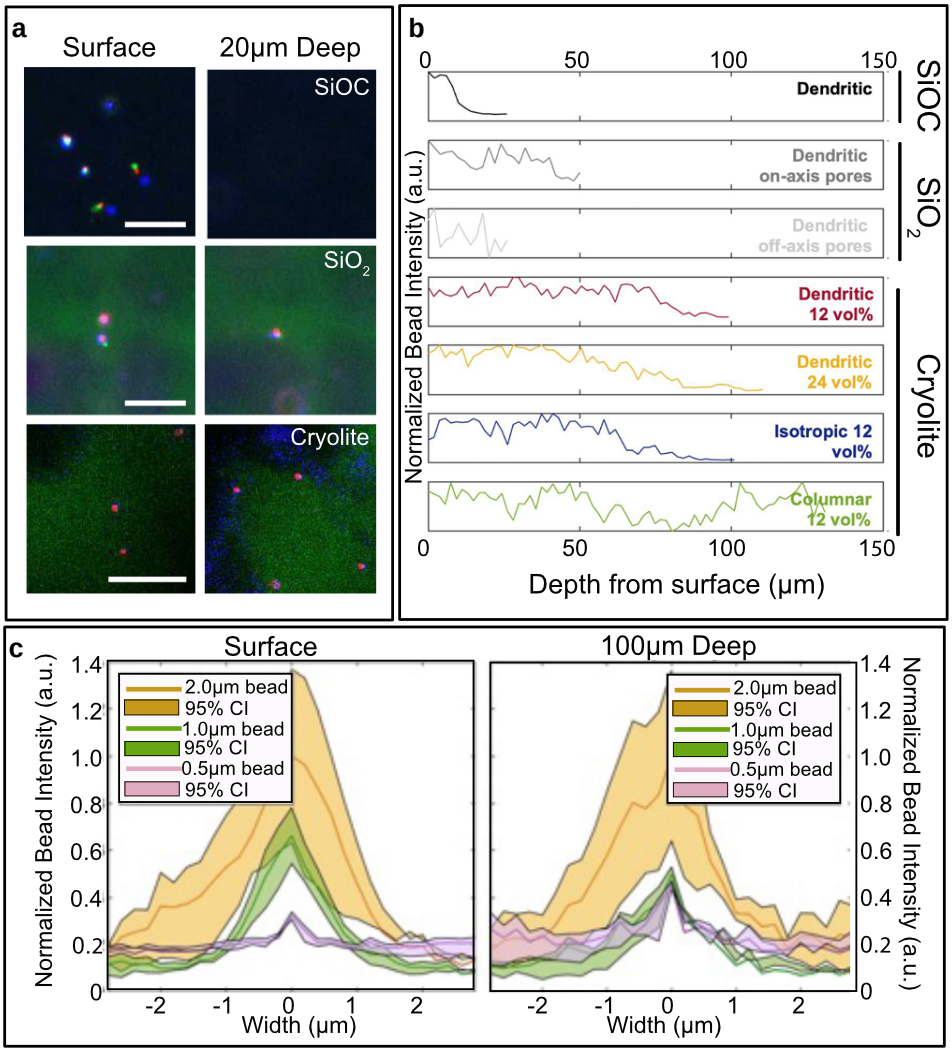

Fig. 3. Comparison of cryolite transparency with other freeze-cast materials using micron-sized fluorescent beads. a) Confocal microscopy images of fluorescent beads at the surface (0 μm) and at 20 μm depth within scaffolds composed of SiOC, SiO_2, and cryolite. Scale bar is 25 μm in each. b) The intensity of bead fluorescence (1 μm diameter), normalized to the maximum bead brightness and shown as a function of depth for the four cryolite scaffold morphologies. A comparison of bead brightness in scaffolds of SiOC and SiO_2 is shown. The intensities of 10 beads were averaged at each depth until the fluorescent beads were no longer visible (<20 μm in the case of SiOC). c) Lateral intensity profiles of 0.5, 1, and 2 μm diameter beads at the surface and at 100 μm depth in the cryolite scaffold with 95% CIs indicates cell-sized particles as small as 0.5 μm can still be confidently resolved to at least 100 μm depth.

saturated (Fig. 3a), were only visible a few microns from the surface of the sample, and visibility abruptly decreased at ~10 μm from the surface of the sample. Freeze-cast SiO_2, conversely, was slightly transparent when saturated with water. Beads imaged within SiO_2 pores parallel to the imaging direction remained visible to a depth of ~50 μm, whereas those in nonparallel pores were visible only up to 25 μm. This indicates that transparency is influenced not only by RI matching but also by pore orientation (see (40) for further discussion).

In contrast, the analysis of fluorescent beads in the freeze-cast cryolite showed high visibility and brightness in all scaffold morphologies. In the saturated 12 vol.% dendritic cryolite scaffolds, beads were routinely imaged at an average depth of 75 μm, with some detected to depths of 100 μm. Similar results were obtained with the denser 24 vol.% dendritic and isotropic cryolite samples, which suggests that bead visibility in saturated cryolite is not wholly dependent on pore size or orientation. In the columnar scaffolds, beads were visible at depths >130 μm from the surface of the sample (Fig. 3b).

As microbes have an average size of 0.5–2.0 μm, we also characterized the ability to accurately resolve similar sized particles deep within the cryolite scaffolds. Figure 3c shows the lateral intensity profiles of 0.5, 1.0, and 2.0 μm FITC-fluorescent beads at the surface (0 μm) and at 100 μm depth for a dendritic cryolite scaffold. All three bead sizes were readily resolved in the cryolite to a depth of 100 μm. This suggests that fluorescently labeled microorganisms of sufficient brightness as small as 0.5 μm in diameter can be detected within the scaffolds.

Particle tracking in cryolite structures

Ideally, microorganisms colonizing the scaffolds could be directly tracked using live cell imaging. To test this capability, we assessed the effect of pore size, morphology, and connectivity on the movement of microbe-sized particles within cryolite scaffolds by conducting confocal microscopy time-lapse imaging of 1 μm FITC-fluorescent beads in saturated solution. In Fig. 4a–d, representative confocal microscopy images are shown for each pore

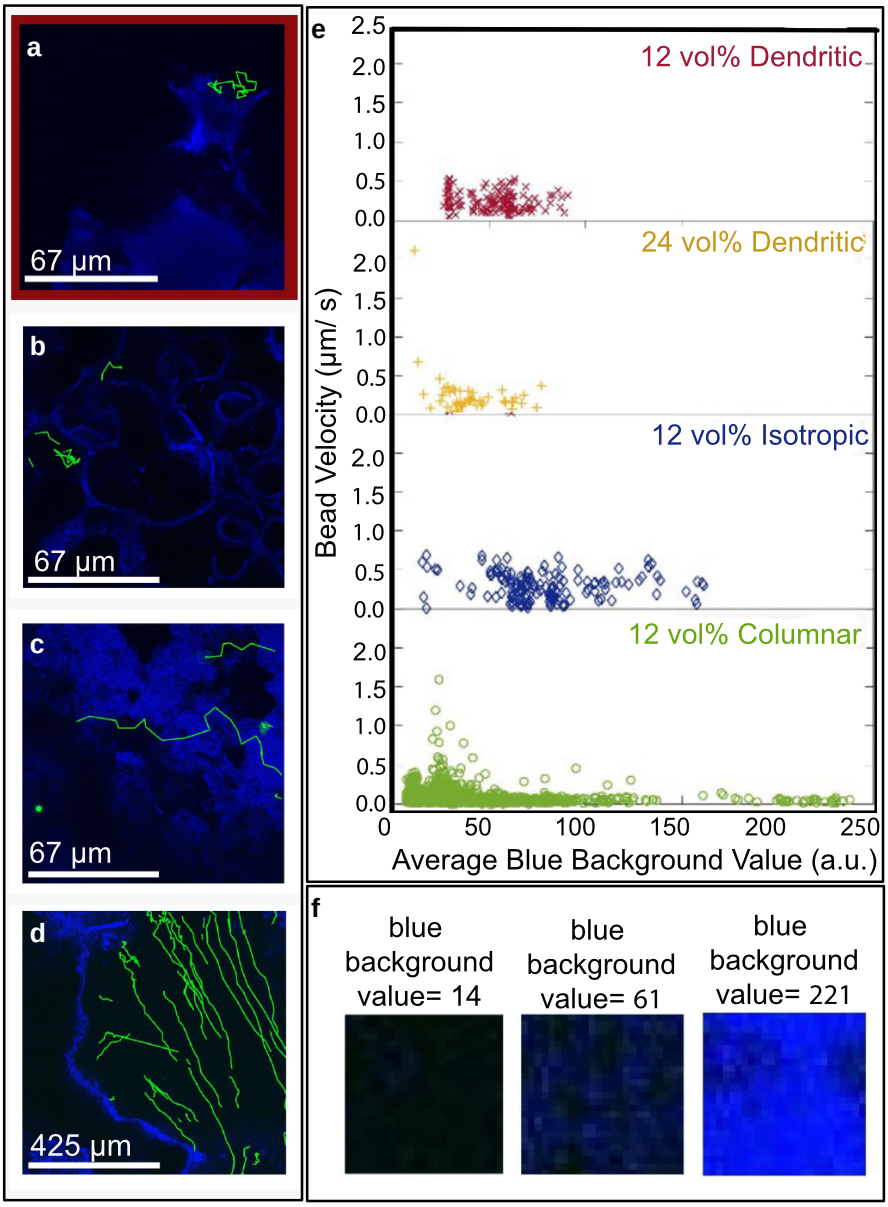

Fig. 4. Tracking the movement of cell-sized fluorescent beads within different scaffold morphologies. Traces of the travel paths for 1 μm beads were visualized every 20 s over a 10-min period and overlaid on fluorescent (405 nm) confocal microscopy images for a) 12 vol.% dendritic, b) 24 vol.% dendritic, c) 12 vol.% isotropic, and d) 12 vol.% columnar porous cryolite scaffolds. In all images, the open-pore space is black, and the cryolite scaffold material appears blue due to some autofluorescence of cryolite in the UV range when excited by a 405-nm laser. e) The velocity of all measured 1 μm beads in each scaffold plotted against the intensity of blue pixels in the 25 × 25 pixel area surrounding each bead (with blue intensity serving as a proxy for the cryolite scaffold versus black open-pore space). f) Blue background intensities (a.u.) for representative 25 × 25 pixel areas with open-pore space showing low (blue background = 14 a.u.), medium (blue background = 61 a.u.), and high regions of cryolite (blue background = 229 a.u.) used in (e).

morphology with the path traveled for individual fluorescent beads overlaid in green (see Materials and methods). In both 12 and 24 vol.% dendritic pore morphologies, beads were confined to areas just off the primary dendrite arms (Fig. 4a and b). These constrained movements originate from beads trapped in secondary arms, and movement appeared limited to these regions. Conversely, within the isotropic pore network (Fig. 4c), beads moved through the sponge-like pore network, rather than remaining trapped in certain pore spaces within the scaffold. Columnar pore morphologies showed beads moving in one direction across the pore space before striking the pore wall and bouncing off (Fig. 4d). Unlike beads in the dendritic isotropic pore networks, they remained exclusively in the highly aligned pores.

These qualitative observations were confirmed by quantitative analysis of the area around the beads as they moved throughout the transparent cryolite scaffold (Fig. 4e and f). Since cryolite is slightly autofluorescent in the UV range, cryolite-dense regions excited by a 405-nm laser appeared as brighter blue on the image, while more porous regions appeared as black (Fig. 4f). Similarly, high-blue intensity values correspond to areas of high cryolite content, while low-blue intensity corresponds to highly porous regions of the sample (Fig. 4f), which means that bead location (cryolite dense or open pore) can be estimated microscopically.

When bead velocity was plotted against the blue background intensity (autofluorescence) around each bead, different behaviors were apparent across the three classes of morphologies

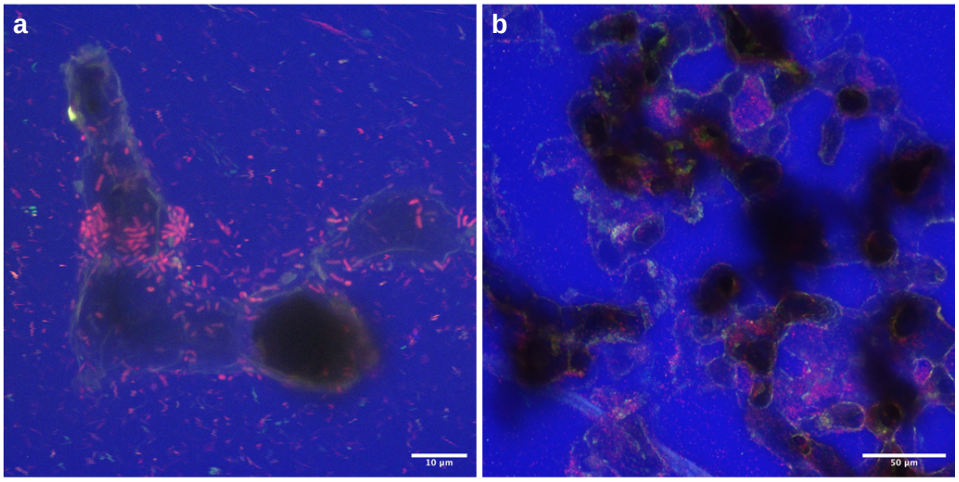

Fig. 5. Microbial compatibility with freeze-cast synthetic cryolite. a) Confocal z-stack image showing a maximum intensity projection of a dendritic cryolite scaffold colonized by a cultured bacteria (*Pseudoalteromonas*) expressing a far-red fluorescent protein. The gray and black regions represent the cryolite mineral grains, while blue shows the saturated pore space within the scaffold (pore space was stained with a 0.0001% fluorescein solution and false colored blue in the image). A view of the same area under low (10×) magnification is shown in (b). Scale bar is 10 µm in panel (a) and 50µm in panel (b). Images of the individual channels are provided in Fig. S2.

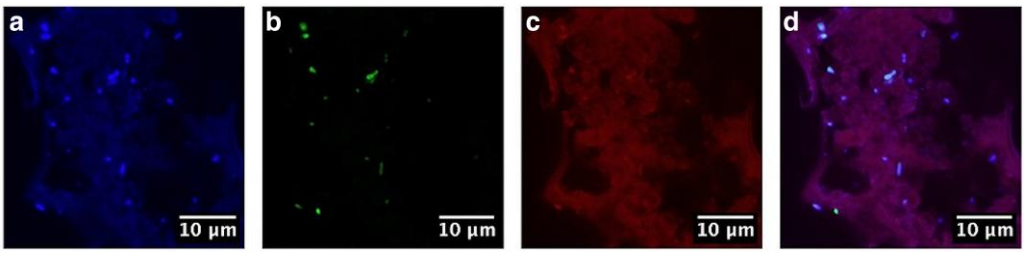

Fig. 6. Freeze-cast cryolite is compatible with FISH. Confocal image of a 12 vol.% dendritic cryolite scaffold colonized by a bacterial co-culture of *P. carrageenovora* and *R. nubinhibens*. Cells were fixed with paraformaldehyde and then hybridized with the general bacterial oligonucleotide probe, Eub338mix labeled with Alexa 488 and counterstained with the DNA stain DAPI (panels b and a). The passive dye AlexaFluor647 was additionally added to the aqueous solution visualize the pore structure (panel c). The overlay of the individual channels is displayed in (panel d). A negative control for FISH of the same co-culture without the addition of Eub338 is provided in Fig. S3.

(Fig. 4e). In dendritic pore networks, beads moved into side channel pores near the main channel so that the area around these beads was generally not highly autofluorescent. In isotropic networks, however, beads moved in regions of higher background intensities. This indicates that fluorescent beads move within the sponge-like pore network where cryolite (increased blue autofluorescence) is partially obstructing the field of view. However, as the cryolite and aqueous medium have matching RI, these beads remained visible even as they moved throughout the complex, tortuous pore scaffold. Finally, beads in columnar pore networks mostly resided in regions with even lower autofluorescence —corresponding to the highly aligned columnar pores (i.e. with no cryolite obstructing the field of view nor the beads' movement). When beads in columnar scaffolds approached denser cryolite areas with higher background values, their velocities slowed or halted as the beads hit the dense pore walls. The documented variation in bead movement within the dendritic, isotropic, and columnar scaffolds illustrates the potential for 3D, real-time tracking of colonization and transport behavior of fluorescent microorganisms over time. We note that all bead movements in this study were only driven by the pressure of the confocal microscope objective on the coverslip, and their movement is due to flow through the larger pores, not from capillary forces in the smaller pores. Placing such scaffolds in a controlled flow system, such as one connected to a peristaltic or syringe pump, would allow for observation of microbes or microbe-sized particles under different flow regimes.

Microbial compatibility assessments of freeze-cast cryolite

The cryolite freeze-casting process incorporates the use of organic solvents, which could inhibit microbial growth. To test the microbial compatibility and colonization potential of cryolite scaffolds, we used an aerobic heterotrophic bacterial strain (*Pseudoalteromonas* sp.) that was genetically modified to express a plasmid (pBTK569) with the far-red fluorophore E2-Crimson. Incubation of the cryolite scaffold with fluorescent bacteria showed dense colonization of the pore space within a day (Figs. 5 and S2). Close inspection revealed localized areas with attached bacterial biofilms within the cryolite pore space, as well as planktonic cells within the infiltration media, shown in blue. The cells in this experiment were imaged live, validating the potential for observation of microbial behavior and colonization patterns. With a fluorescently labeled or autofluorescent strain, microorganisms can be imaged in real time or studied at set time points over the course of the experiment. This would allow for real-time examination of the effects of nutrient addition, or changes in

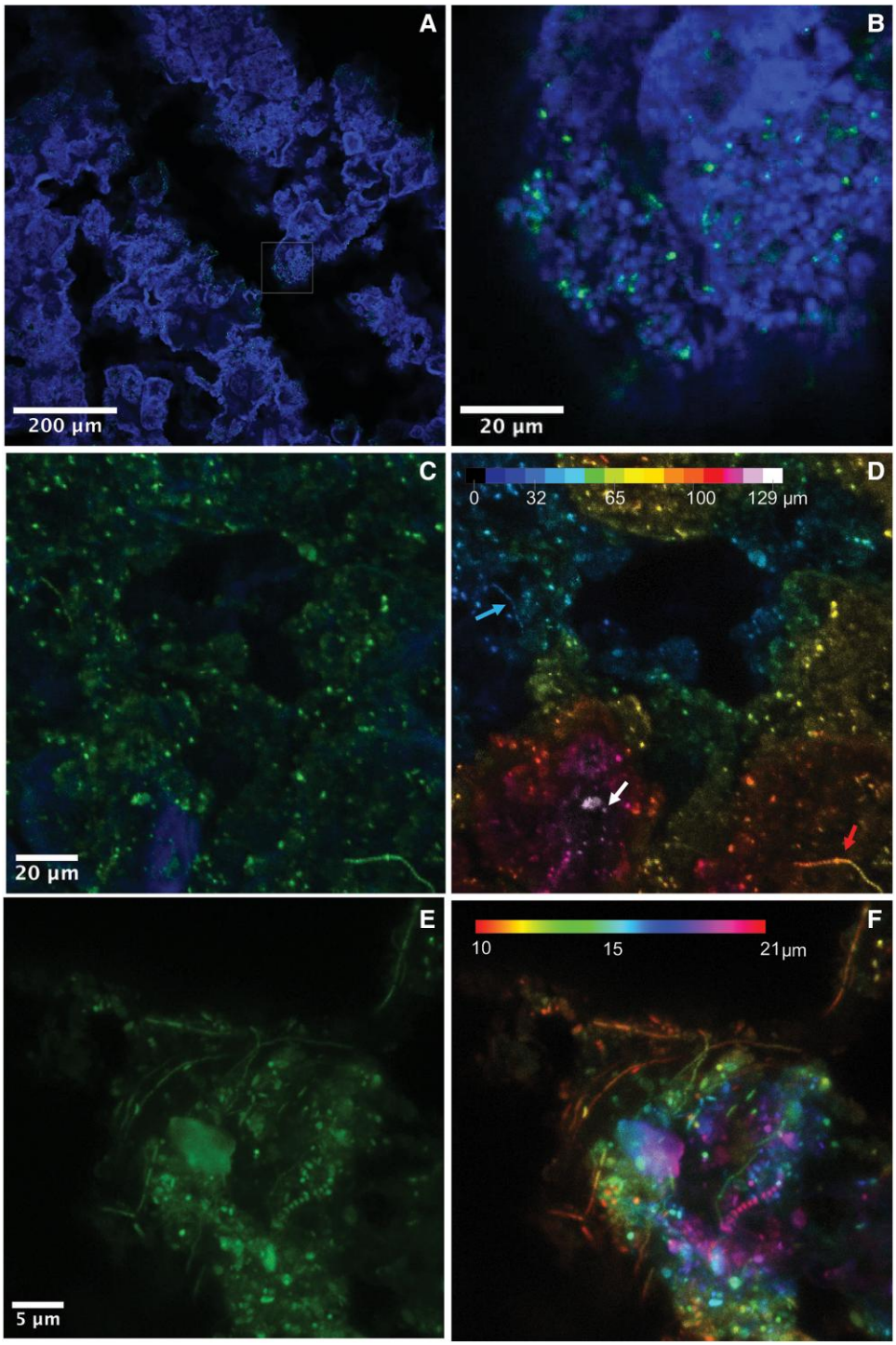

Fig. 7. Environmental deployment of a cryolite scaffold shows robust in situ microbial colonization deep into the cryolite pore network. A 12 vol.% dendritic cryolite scaffold was directly inserted into seagrass rhizosphere sediment for 4 weeks, fixed in paraformaldehyde, and colonizing microorganisms stained with the nucleic acid stain SYBR Gold. Confocal microscopy maximal depth projections at 10× (panels a–d) and 100× (panels e and f) magnification. a) The cryolite matrix (blue autofluorescence) and open-pore space (black) and b) a magnification of the inset box in (a), showing SYBR-stained environmental microorganisms (in green) within the cryolite matrix (blue). Cells were visible even at low magnification (10×) and deep within the scaffold (85 µm depth, still frame taken from Video S2a). c) A maximum intensity projection (MIP) of a 129-µm z-stack (associated with Video S2b, representing an overlay of DAPI and FITC channels and d) the corresponding color-coded depth projection (CCP) of the same image showing environmental microorganisms distributed at multiple depths throughout the scaffold. The color scale of the CCP represents depth, with each color bar representing 8.08 µm increments. Filamentous cells marked with a blue arrow span 32 to 40 µm depth, while filamentous cells on the right with the red arrow were located deeper in the scaffold, between 80 and 100 µm. Single cells were resolved as deep as 125 µm (white arrow). Using a 100× objective allows higher resolution images of cells within the cryolite matrix, but at comparatively shallower depths due to the smaller depth of field of the objective. e) A higher magnification MIP (FITC channel only showing SYBR-stained cells) and corresponding (f) CCP of an 11-µm z-stack (Video S3) collected with a 100× objective show well-resolved cells of various morphologies, including fine filamentous cells, thicker chains of cells, single bacilli, and cocci. The color scale bar of CCP begins at 10 µm to indicate that imaging did not begin at the coverslip (0 µm) but deeper into the matrix, from 10 to 21 µm. Individual channel images are provided in Fig. S4.

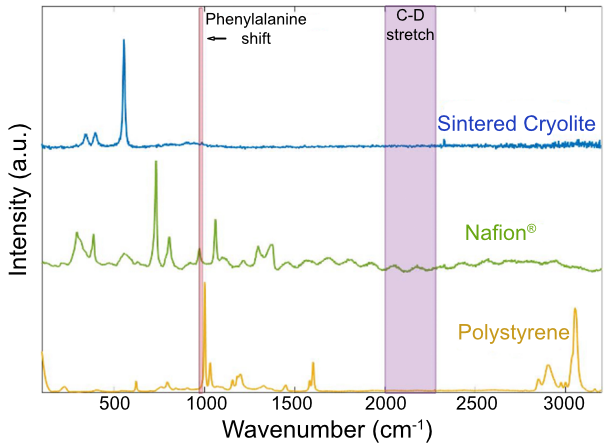

Fig. 8. Raman spectra of sintered synthetic cryolite, Nafion, and polystyrene, highlighting regions used for single-cell stable isotope probing with ^{13}C-labeled substrates or D_2O. Freeze-cast synthetic cryolite has low background in regions used for ^{13}C (phenylalanine shift) and deuterium detection in cells (C-D stretch), offering an advantage over other commonly used TS materials like Nafion and polystyrene. The pink-shaded areas represent regions used for detecting ^{13}C (966 and 1,003 cm^{-1}) and deuterium (2,030—2,300 cm^{-1}) incorporation by microorganisms.

environment on the spatiotemporal colonization and activity of microbes within the porous scaffold.

The cryolite scaffolds were also compatible with endpoint analyses including fluorescence in situ hybridization (FISH), which allows the visualization of bacterial cells. A cryolite scaffold was incubated with a bacterial co-culture containing *Pseudoalteromonas carrageenovora* and *Roseovarius nubinhibens*. FISH assays on the colonized scaffold using the general bacterial 16S rRNA oligonucleotide probe (EUB338mix) counterstained with the DNA stain DAPI revealed strong correspondence between cells observed with DAPI and those positively hybridized by the FISH probe. This included cells that had colonized deep within the interior of the cryolite scaffold, indicating successful penetration of the probe mix (Fig. 6). The negative FISH control confirmed a low fluorescence background under the FITC filter set (green fluorescence channel), indicating minimal autofluorescence from the cryolite matrix (Fig. S3). This proof-of-concept FISH experiment demonstrates the compatibility of the freeze-cast cryolite scaffolds with fluorescence staining methods. Combining taxon-specific FISH probes will enable the targeting of multiple microbial groups while preserving critical information about their spatial structure within the scaffold.

One of the greatest bottlenecks in our understanding of microbes living belowground is our inability to observe them in situ. To test the robustness of these scaffolds for direct deployment in the field, we inserted a dendritic scaffold directly into rhizosphere sediments of a living coastal eelgrass plant (*Zostera marina*) maintained in a marine laboratory aquarium and recovered the dendritic scaffold after 4 weeks of incubation in situ. The recovered cryolite scaffold was immediately fixed with paraformaldehyde, washed, and stained with the nucleic acid stain SYBR Gold, followed by confocal microscopy imaging to depths of about 130 µm (Figs. 7 and S4, Videos S1 and S2). The cryolite scaffold exhibited some autofluorescence under UV (Fig. 7, DAPI channel). However, even at low 10× magnification, a high density of environmental microorganisms was visible throughout the cryolite scaffold at multiple depths (Fig. 7, top and center rows, Video S1).

Confocal imaging using a low magnification 10× objective enabled the imaging of large regions (850 µm per field of view) and regions deep in the scaffold (~130 µm deep). Zooming into these images reveals microbes resolved at the level of single cells, even up to 125 µm into the matrix. Orthogonal views show single cells cleanly resolved even in the z-dimension at 80 µm depth (Fig. S5). Even higher resolution images were obtained by using a 100× objective. However, the 100× objective is limited to smaller fields of view (85 versus 850 µm for 10× objective) and shallower imaging due to its intrinsically smaller depth of field (0.43 µm for 100× objective, versus 4.04 µm for 10× objective).

Video S2 shows a z-stack of the scaffold imaged under 100× magnification. Over the full 11 µm imaged in the z-stack, diverse microbes are apparent at high resolution, including rod-shaped, coccoid, filamentous, and cable-like bacteria, like the morphological diversity we previously observed by FISH in the analyses of microbial samples of the seagrass rhizosphere and sediment. The observation of a variety of cell morphologies and sizes colonizing the cryolite scaffold during the sediment incubation highlights the broad range of native environmental microbes capable of entering and inhabiting these transparent rock and sediment experimental analog systems.

Potential for microbial analysis using Raman microspectroscopy techniques

While visualizing and identifying microbes in complex porous scaffolds is an important advance, cryolite scaffolds also have the potential to be used for quantifying microbial activities in belowground ecosystems, using Raman microspectroscopy and single-cell stable isotope probing techniques. This largely nondestructive method enables the direct tracking of single-cell activity and metabolic potential over time. The technique can be combined with FISH to quantify deuterated water (D_2O)- and ^{13}C-labeled substrate assimilation by single microbial cells (43–47). Raman-based determination of stable isotope enrichment in cells relies on the shifting of peaks between 966 and 1,003 cm^{-1}, or 2,030 and 2,300 cm^{-1}, for D_2O- and ^{13}C-labeled substrates, respectively. Nafion, polystyrene, and natural cryolite exhibit no interference peak around 2,030 and 2,300 cm^{-1}, and the uptake of D_2O into cell biomass can therefore be used as a proxy for anabolic activity with these materials. However, Nafion and polystyrene present interference peaks around 966 and 1,003 cm^{-1}, limiting the ability to track specific carbon substrate use (44, 45, 48–50) (Fig. 8). The natural form of cryolite has no interferences in this region and has been successfully used in Raman-based stable isotope probing of ^{13}C-glucose assimilation by *Bacillus subtilis* (17). While the off-the-shelf synthetic cryolite produced Raman peaks throughout the spectrum due to its amorphous (noncrystalline) structure, the sintering technique used in this study generates a heat-treated form of cryolite with a Raman spectrum that closely resembles the crystalline form, with a single sharp peak and smooth baseline (Fig. 1d). This indicates compatibility of the cryolite scaffolds for conducting multimodal analyses of microbial communities, where fluorescence analysis and Raman-based stable isotope probing with ^{13}C and deuterium can be combined on individual microbes.

Conclusion

In this study, we have introduced a facile method for creating optically transparent, microbially compatible, tunable, and deployable porous scaffolds by freeze-casting inexpensive synthetic

cryolite mineral powder. The method allows reproducible production of transparent rock and sediment analogs with controlled pore sizes, orientations, and geometries, and represents an innovative tool for studying the effects of these parameters on the colonization, growth, physiological activity, interactions, and community structure of microorganisms in either a lab or field setting.

This technology suggests several possible extensions. Cultured or environmental microbes may be incubated in cryolite scaffolds with the metabolic activity markers such as redox sensor green (51), or "clickable" methionine analogs, azidohomoalanine (AHA) or L-homopropargylglycine (HPG), for use in biorthogonal noncanonical amino acid tagging (BONCAT (52, 53)) assays to identify spatial patterns in microbial activity according to pore space characteristics. Cryolite surfaces may be chemically functionalized to produce a variety of surface properties reproducing different mineral types—for example, iron oxyhydroxide treatment to produce charged iron surfaces and observe the effect of treatment on microbial habitation (54). Similarly, Patko et al. (55) functionalized a fluorinated ethylene propylene (FEP)-based transparent soil (TS) with pH sensors to produce a "smart" pH-sensitive TS scaffold, suggesting a possible extension in this direction for cryolite. The optical transparency of cryolite scaffolds also makes them potentially compatible with laser ablation, dissection, or optical tweezer capabilities, enabling precise micromanipulation of individual microbes and communities, including their introduction or removal from the sample (17,56, 57). Imaging scaffolds with two- and three-photon imaging should additionally extend the potential depth of resolution to hundreds of micrometers, well beyond the ~100 µm range we have demonstrated here using standard confocal microscopy (58). Finally, our demonstration that the cryolite scaffolds are compatible with Raman spectroscopy for measuring ^{13}C- and D_2O-labeled microbes invites the design and execution of stable isotope probing experiments for tracking carbon flows and microbial anabolic activity within in situ incubation experiments. As the need for a mechanistic understanding of belowground chemistry, microbiology, and the associated physical environment grows, powerful matrices such as the freeze-cast cryolite scaffolds presented here are an important and timely development in these fields of research.

Materials and methods

Freeze casting of cryolite

Cryolite suspensions were prepared for four pore morphologies according to the parameters detailed in Table 1. The dispersant (KD4; Croda Inc., Snaith, UK) was sonicated with the cyclohexane solvent until fully dissolved before cryolite (PyroChemSource, Hayward, MN, USA) was added according to the quantities listed in Table 1, and the suspension was ball milled until thoroughly mixed. The suspension was then pipetted into a borosilicate mold on a thermoelectric cold plate (Fig. 1a (18, 59)) for freeze casting. Once freeze cast, the samples were left in a lyophilizer (VirTis AdVantage 2.0; SP Scientific, Warminster, PA, USA) for at least 24 h. The samples were then sintered, uncovered, in air using a box furnace (CM Rapid Temp 1700 °C Furnace; CM Furnaces, Inc., Bloomfield, NJ, USA) for 2 h at 600 °C to burn off any residual organic compounds before sintering at 900 °C for 6 h in an Ar atmosphere in a tube furnace (Carbolite CTF 17/300 Tube Furnace; Carbolite Gero, Sheffield, UK).

Preparation of cryolite scaffolds

For ease of handling, labeling, and imaging, cross-sections of the freeze-cast cryolite scaffolds were prepared by immersing the coupons in a low-shrinkage acrylic (VariDur3003; Buehler, Lake Bluff, IL, USA) to surround the cryolite scaffolds and enable easier machining into disks. Once the acrylic was fully hardened, the samples used for culturing and imaging were sliced into 2 mm high disks using a diamond saw. Samples for porosimetry measurements were not immersed in acrylic.

Chemical and pore morphology characterization

Synthetic cryolite powder was exposed to the same range of temperatures and times used in producing the freeze-cast scaffolds. The process of freeze casting this synthetic cryolite includes two sintering steps: one at 600 °C to burn away any residual suspending or binding agents used in the freeze-casting process, and one at 900 °C which densifies and strengthens the freeze-cast porous scaffold. While the first sintering step must take place in air to fully burn off organic residues which may compromise the transparency of the final cryolite scaffold, the higher temperature heat treatment must take place in an inert environment (e.g. under argon) to prevent oxidation of the cryolite crystals. The cryolite was then analyzed using Raman spectroscopy (Renishaw InVia Raman Microscope) to characterize any chemical degradation that took place because of the heat treatments needed to densify the freeze-cast materials. A 514-nm laser and 50× lens were used to scan 400 locations across the samples; those spectra were then averaged to assess the spectral character of the sample as a whole. To characterize the pore size distribution of scaffolds, mercury intrusion porosimetry was carried out using a Micromeritics AutoPore IV Mercury Intrusion Porosimeter. To validate reproducibility between batches, two 12 vol.% dendritic samples that were freeze cast at different times were each characterized using mercury intrusion porosimetry, producing similar pore size distributions (Fig. S6). SEM was performed using a Zeiss 1550VP scanning electron microscope housed in the Division of Geological and Planetary Sciences at Caltech, and images were processed using ImageJ (National Institutes of Health). At least three samples of each morphology were prepared and imaged using SEM, and representative images were selected for presentation in this work.

Confocal imaging with fluorescent beads

Two solutions were prepared for imaging pore spaces under confocal microscopy: (i) a solution of nanopure water, 0.05% fluorescein (Sigma-Aldrich), and 1% of 1 mm TetraSpeck Beads (ThermoFisher) and (ii) a solution of nanopure water, 0.05% AF647 (ThermoFisher), and 1% each of 0.5, 1, and 2 µm green fluorescent beads (Flow Cytometry Size Particle Reference Kit; ThermoFisher). TetraSpeck beads were only used in fluoroscein solutions, and green fluorescent–only beads were only used in solutions of AF647. Scaffold cylinders sliced into 2 mm thick rounds were saturated with water overnight to allow time for the water to fully permeate. The next day, a few drops of the water/fluorescein/bead solution were placed on the sample and covered with a coverslip immediately prior to imaging. Samples were imaged using a LSM880 Confocal Microscope (Carl Zeiss AG, Oberkochen, Germany) and 10× Plan-Apochromat 0.45 M27 and 100× alpha Plan-Apochromat 1.46 Oil DIC M27 objectives in the Beckman Institute Biological Imaging Center (Caltech) to produce z-stacks. Bead intensities from these images were analyzed using FIJI (National Institutes of Health) and MATLAB. For pore morphology characterization and transparency depth assessments (Figs. 2 and 3b), a solution with 1 µm TetraSpeck beads was used, *and* the intensities of 10 beads per depth from the sample surface were tracked over at least three regions of each cryolite sample.

To produce lateral intensity profiles (Fig. 3c), beads from the Flow Cytometry Size Kit were used. Tracking of bead movement within scaffolds of different pore morphologies was conducted with the same confocal microscope by maintaining a constant focal plane and collecting images every 20 s over a 10-min period.

Cryolite scaffold inoculation with a fluorescently labeled live cell culture

The marine *Pseudoalteromonas* sp002723455 transformed with plasmid pBTK569 expressing the far-red fluorophore E2-Crimson was cultured on MB-spectinomycin agar (100 μg/mL) at 28 °C for 48 h. This strain and all cultured strains used in this study were provided by the Cordero Lab (Massachusetts Institute of Technology, Cambridge, MA, USA). A single colony was transferred to liquid MB-spec and grown overnight at 28 °C shaking. Fifty microliters of the overnight culture were diluted 1:100 in 5 mL MB-spec to a final cell density of $OD_{600} = 0.3$. In addition, 5 μL of 0.1% fluorescein was added as a passive fluorescent tracer (to a final concentration of 0.0001% fluorescein). A cryolite scaffold (dendritic pore morphology, 12% solids loading) was sterilized by immersion in 70% ethanol for 30 min, and then placed at 80 °C for 5 min to evaporate off the ethanol. The sterilized sample was placed into a 10-mL Petri dish with 5 mL of the cell culture and fluorescein solution. The Petri dish was wrapped in foil to protect it from light and incubated at room temperature overnight. The scaffold was then transferred onto a sterilized coverslip, and fresh MB-spec broth with 500 μL of 0.0001% fluorescein was added to maintain hydration and maintain cell viability. The sample was then immediately imaged by confocal microscopy in Caltech's Beckmann imaging center. All confocal images were acquired using an upright Zeiss 880 CLSM (Zeiss, Oberkochen) using 10× or 100× objectives (Plan-Apochromat 10×/0.45 M27 and alpha Plan-Apochromat 100×/1.46 Oil DIC M27 objectives).

FISH within cryolite scaffolds

Pseudoalteromonas carrageenovora and *R. nubinhibens* strains originally isolated from coastal seawater (60) were cultured on marine broth (MB) agar at 28 °C for 48 h. Both cultures were grown in MB broth from single colonies at 28 °C shaking overnight. *Pseudoalteromonas carrageenovora* was diluted to $OD_{600} = 0.01$, and *R. nubinhibens* was diluted to $OD_{600} = 0.1$ in sterile MB broth (to account for the larger size and higher growth rate of *P. carrageenovora*). A volume of 2.5 mL of each culture was then mixed (5 mL total) and the co-culture added to a sterile 10 mL Petri dish. Two sterilized cryolite scaffolds, as described above, were added to the Petri dish containing the co-culture, and incubated overnight at 28 °C.

After incubation with the co-culture, both scaffolds were removed using sterile tweezers and placed in a separate Petri dish containing 4 mL of 4% paraformaldehyde fixative and incubated at 4 °C overnight to preserve the cells. Scaffolds were then washed by immersion in 5 mL of 3× PBS at room temperature for 10 min; the wash was repeated with fresh PBS. Scaffolds were then transferred into a solution of 1:1 PBS:ethanol for 30 min at room temperature to dehydrate the cells, followed by a drying step at 80 °C for 30 min (samples were turned over after 15 min to completely dry both sides).

FISH hybridization solution containing 35% formamide and the general bacterial EUB388-dual_Alexa488 probe set (61) was prepared as follows: 400 μL total volume, 72 μL 5 M NaCl, 7.5 μL 1 M Tris/HCl, 136 μL nanopure water, 140 μL formamide, 4 μL 1% SDS, and 40 μL EUB388 probe mix. The Eub probe mix contained equal volumes of EUB388I, EUB388II, and EUB388III probes (50 ng/μL probe total). After the fixation and dehydration steps, the scaffold was placed in 400 μL of hybridization solution in a 0.6-mL eppendorf tube, and the second scaffold was placed in an identical solution without probes (serving as a negative control to check for background autofluorescence, where the equivalent probe volume was substituted with nanopure water). Both scaffolds were hybridized overnight at 46 °C. Samples were then washed in 2 mL of FISH wash buffer (70 mM NaCl, 20 mM Tris/HCl, 5 mM EDTA) in 2 mL eppendorf tubes for 10 min in a 48 °C water bath. Following the wash step, scaffolds were briefly dipped in nanopure water and dried under a gentle stream of air and then placed in a closed Petri dish in the dark at room temperature to complete the drying process. FISH-hybridized scaffolds were subsequently mounted on a coverslip with 500 μL of anti-fade Citifluor solution containing the general DNA stain DAPI (4.5 mg/mL final concentration). Samples were then imaged with confocal microscopy as described above.

Environmental deployment and SYBR Gold nucleic acid staining

A sterilized cryolite scaffold was buried ~1 cm below the sediment surface, touching the roots of a coastal *Z. marina* plant that had been transplanted into an aquarium at Kerckhoff Marine Laboratory (Corona del Mar, CA, USA). The healthy plant and surrounding sediment had been collected 1 month earlier from a seagrass meadow just offshore of Caltech's Kerckhoff Marine Laboratory. The scaffold was left buried in the aquarium sediments for 4 weeks, then retrieved, fixed in paraformaldehyde, and washed following the FISH protocol described above. Colonizing microorganisms were then stained with 250 μL of 25× of the general nucleic acid stain SYBR Gold (ThermoFisher Scientific) and incubated at room temperature in the dark for 10 min. A solution of AlexaFluor647 NHS Ester (ThermoFisher Scientific) was also added at a final concentration of 1 μg/mL, serving as a passive tracer for tracking liquid penetration and visualizing pore morphology. The cryolite scaffold containing the SYBR Gold plus AF647 solution was then transferred to a glass slide, covered with a coverslip, and imaged with confocal microscopy as described above.

Acknowledgments

The authors thank Julia Schwartzman and Otto Cordero (MIT) for providing the bacterial strains used in this study, Shaelyn Silverman (Caltech) for assistance with bacterial cultivation, George Rossman (Caltech) for use of his Raman instrument, Julie Kornfield for inspiration and discussions about this work, Emmanuelle Botté (Manuscribe) for editorial assistance, and two anonymous reviewers whose suggestions improved this manuscript. The authors additionally acknowledge Caltech's Kerckhoff Marine Laboratory for facility support and access to the seagrass field site. Collection of *Z. marina* sediment cores for incubation experiments was carried out under permit ID SC-13962 issued from the State of California–Department of Fish and Wildlife. V.J.O. is a CIFAR Fellow in the Earth 4D Subsurface Science and Exploration program.

Supplementary Material

Supplementary material is available at *PNAS Nexus* online.

Funding

This work was supported through a collaborative pilot research grant from the Caltech's Donna and Benjamin M. Rosen Bioengineering Center (ROSENBE.PROJECTS-6.VJO-ENDOW.ROSENBE to K.T.F. and V.J.O.) as well as support from the US Department of Energy, Office of Science, Office of Biological and Environmental Research under Award Number [DE-SC0022991], from the Simons Foundation Principles of Microbial Ecosystems (PriME) consortium (V.J.O.), and partial support from the Resnick Sustainability Institute (RSI.DIRINIT-VJO-RESNICK.SRA; to V.J.O.).

Author Contributions

Laura K. Quinn (Resources, Data curation, Formal analysis, Investigation, Visualization, Methodology, Writing—original draft), Kriti Sharma (Supervision, Validation, Investigation, Visualization, Methodology, Writing—original draft), Katherine T. Faber (Conceptualization, Supervision, Funding acquisition), and Victoria J. Orphan (Conceptualization, Supervision, Funding acquisition, Investigation, Methodology, Project administration, Writing—review & editing).

Data Availability

The authors confirm that the data supporting the findings of this study are available within the article and its Supplementary material. The raw data files are openly available in Figshare at https://doi.org/10.6084/m9.figshare.27173274.v1.

References

1 Templeton AS, Caro TA. 2023. The rock-hosted biosphere. *Annu Rev Earth Planet Sci*. 51:493–519.
2 Pienkowska A, *et al*. 2021. Isotopic labeling reveals microbial methane oxidation coupled to Fe(III) mineral reduction in sediments from an as-contaminated aquifer. *Environ Sci Technol Lett*. 8: 832–837.
3 Anderson RT, *et al*. 2003. Stimulating the in situ activity of Geobacter species to remove uranium from the groundwater of a uranium-contaminated aquifer. *Appl Environ Microbiol*. 69: 5884–5891.
4 Nunan N, Wu K, Young IM, Crawford JW, Ritz K. 2003. Spatial distribution of bacterial communities and their relationships with the micro-architecture of soil. *FEMS Microbiol Ecol*. 44:203–215.
5 Rabot E, Weismeier M, Schüter S, Vogel H. 2018. Soil structure as an indicator of soil functions: a review. *Geoderma*. 314:122–137. doi:10.1016/j.geoderma.2017.11.009.
6 Baveye P, *et al*. 2018. Emergent properties of microbial activity in heterogeneous soil microenvironments: different research approaches are slowly converging, yet major challenges remain. *Front Microbiol*. 9. doi:10.3389/fmicb.2018.01929.
7 Cholodny N. 1930. Ober eine neue methode zur untersuchung der bodenmikroflora. *Arch Mikrobiol*. 1:620–652.
8 Zobell CE, Allen EC. 1933. Attachment of marine bacteria to submerged slides. *Proc Soc Exp Biol Med*. 30:1409–1411.
9 Deng J, *et al*. 2015. Synergistic effects of soil microstructure and bacterial EPS on drying rate in emulated soil micromodels. *Soil Biol Biochem*. 83:116–124.
10 Bhattacharjee A, *et al*. 2020. Visualizing microbial community dynamics via a controllable soil environment. *mSystems*. 5(1): e00645-19. doi:10.1128/msystems.00645-19.
11 Aleklett K, *et al*. 2018. Build your own soil: exploring microfluidics to create microbial habitat structures. *ISME J*. 12:312–319.
12 Aufrecht J, *et al*. 2022. Hotspots of root-exuded amino acids are created within a rhizosphere-on-a-chip. *Lab Chip*. 22:954–963.
13 Stanley CE, Grossmann G, i Solvas XC, deMello AJ. 2016. Soil-on-a-chip: microfluidic platforms for environmental organismal studies. *Lab Chip*. 16:228–241.
14 Nichols D, *et al*. 2010. Use of ichip for high-throughput in situ cultivation of "Uncultivable" microbial species. *Appl Environ Microbiol*. 76(8):2445–2450. doi:10.1128/AEM.01754-09.
15 Iskander M, Bathurst RJ, Omidvar M. 2015. Past, present, and future of transparent soils. *Geotech Test J*. 38:557–573.
16 Ma L, *et al*. 2019. Hydrogel-based transparent soils for root phenotyping in vivo. *Proc Natl Acad Sci U S A*. 116:11063–11068.
17 Sharma K, Palatinszky M, Nikolov G, Berry D, Shank EA. 2020. Transparent soil microcosms for live-cell imaging and non-destructive stable isotope probing of soil microorganisms. *eLife*. 9:e56275.
18 Arai N. *Freeze casting of ceramics: pore design from solidification principles*. California Institute of Technology, 2021.
19 Rooney LM, Dupuy LX, Hoskisson PA, McConnell G. 2024. Construction and characterisation of a structured, tuneable, and transparent 3D culture platform for soil bacteria. *Microbiology*. 170:001429.
20 Downie H, *et al*. 2012. Transparent soil for imaging the rhizosphere. *PLoS One*. 7:e44276.
21 Hancock AM, Datta SS. 2024. Interplay between environmental yielding and dynamic forcing modulates bacterial growth. *Biophys J*. 123:957–967.
22 Chang J, Airey D. 2022. Using transparent soils to observe soil liquefaction and fines migration. *J Imaging*. 8:253.
23 Downie HF, Valentine TA, Otten W, Spiers AJ, Dupuy LX. 2014. Transparent soil microcosms allow 3D spatial quantification of soil microbiological processes in vivo. *Plant Signal Behav*. 9: e970421.
24 Anthony JW, Bideaux RA, Bladh KW, Nichols MC. *Handbook of mineralogy Vol. 3- halides, hydroxides, oxides*. Mineral Data Publishing, Tucson, AZ, 1997. p. 1–145.
25 Berry DA. 2012. Cryolite, the Canadian aluminum industry and the American occupation of Greenland during the Second World War. *Polar J*. 2:219–235.
26 Pauly H, Bailey JC. *Genesis and evolution of the Ivigtut cryolite deposit, SW Greenland*. Museum Tusculanum Press, 1999. p. 1–60 37.
27 Chino Y, Dunand DC. 2007. Directionally freeze-cast titanium foam with aligned, elongated pores. *Acta Mater*. 56:105–113.
28 Mallick KK, Winnett J. 2012. Preparation and characterization of porous bioglass and PLLA scaffolds for tissue engineering applications. *J Am Ceram Soc*. 95:2680–2686.
29 Deville S. Ice-templated materials: polymers, ceramics, metals and their composites. In: Deville S, editor. *Freezing colloids: observations, principles, control, and use: applications in materials science, life science, earth science, food science, and engineering, engineering materials and processes*. Springer International Publishing, 2017. p. 253–350.
30 Zhang H, *et al*. 2005. Aligned two- and three-dimensional structures by directional freezing of polymers and nanoparticles. *Nat Mater*. 4:787–793.
31 Naviroj M, Miller SM, Colombo P, Faber KT. 2015. Directionally aligned macroporous SiOC via freeze casting of preceramic polymers. *J Eur Ceram Soc*. 35:2225–2232.
32 Naviroj M, Wang MM, Johnson MT, Faber KT. 2017. Nucleation-controlled freeze casting of preceramic polymers for uniaxial pores in Si-based ceramics. *Scr Mater*. 130:32–36.

33 Chen R, Wang C-A, Huang Y, Ma L, Lin W. 2007. Ceramics with special porous structures fabricated by freeze-gelcasting: using tert-butyl alcohol as a template. *J Am Ceram Soc.* 90:3478–3484.

34 Faber KT, Kornfield JA, Arai N, Bateman O, Ismagilov RF. Freeze-cast ceramic membrane for size based filtration. 2022 Feb 8. United States patent 11,242,290.

35 Deville S, Saiz E, Tomsia AP. 2006. Freeze casting of hydroxyapatite scaffolds for bone tissue engineering. *Biomaterials*. 27: 5480–5489.

36 Wegst UGK, Schecter M, Donius AE, Hunger PM. 2010. Biomaterials by freeze casting. *Philos Trans A Math Phys Eng Sci*. 368:2099–2121.

37 Xie M, *et al.* 2018. Flexible and active self-powered pressure, shear sensors based on freeze casting ceramic–polymer composites. *Energy Environ Sci*. 11:2919–2927.

38 Shahbazi M-A, Ghalkhani M, Maleki H. 2020. Directional freeze-casting: a bioinspired method to assemble multifunctional aligned porous structures for advanced applications. *Adv Eng Mater*. 22:2000033.

39 Quinn LK. *Freeze-cast porous ceramics: tailoring chemistry and porosity for functionality*. California Institute of Technology, 2024.

40 Wang P, *et al.* 2010. Robust growth of *Escherichia coli*. *Curr Biol*. 20(12):1099–1103.

41 Secchi E, *et al.* 2020. The effect of flow on swimming bacteria controls the initial colonization of curved surfaces. *Nat Commun*. 11(1):2851.

42 Eichorst SA, *et al.* 2015. Advancements in the application of NanoSIMS and Raman microspectroscopy to investigate the activity of microbial cells in soils. *FEMS Microbiol Ecol.* 91:fiv106.

43 Huang WE, Griffiths RI, Thompson IP, Bailey MJ, Whiteley AS. 2004. Raman microscopic analysis of single microbial cells. *Anal Chem*. 76:4452–4458.

44 Huang WE, Ward AD, Whiteley AS. 2009. Raman tweezers sorting of single microbial cells. *Environ Microbiol Rep*. 1:44–49.

45 Berry D, *et al.* 2015. Tracking heavy water (D_2O) incorporation for identifying and sorting active microbial cells. *Proc Natl Acad Sci U S A*. 112:E194–E203.

46 Lee KS, *et al.* 2019. An automated Raman-based platform for the sorting of live cells by functional properties. *Nat Microbiol*. 4: 1035–1048.

47 Li M, Ashok PC, Dholakia K, Huang WE. 2012. Raman-activated cell counting for profiling carbon dioxide fixing microorganisms. *J Phys Chem A*. 116:6560–6563.

48 Li M, Huang WE, Gibson CM, Fowler PW, Jousset A. 2013. Stable isotope probing and Raman spectroscopy for monitoring carbon flow in a food chain and revealing metabolic pathway. *Anal Chem*. 85:1642–1649.

49 Kumar V, *et al.* 2016. Demonstration of carbon catabolite repression in naphthalene degrading soil bacteria via Raman spectroscopy based stable isotope probing. *Anal Chem*. 88:7574–7582.

50 Kalyuzhnaya MG, Lidstrom ME, Chistoserdova L. 2008. Real-time detection of actively metabolizing microbes by redox sensing as applied to methylotroph populations in Lake Washington. *ISME J*. 2:696–706.

51 Hatzenpichler R, *et al.* 2014. In situ visualization of newly synthesized proteins in environmental microbes using amino acid tagging and click chemistry. *Environ Microbiol.* 16:2568–2590.

52 Marlow J, *et al.* 2021. Spatially resolved correlative microscopy and microbial identification reveal dynamic depth- and mineral-dependent anabolic activity in salt marsh sediment. *Environ Microbiol*. 23:4756–4777.

53 Knapp EP, Herman JS, Hornberger GM, Mills AL. 1998. The effect of distribution of iron-oxyhydroxide grain coatings on the transport of bacterial cells in porous media. *Environ Geol*. 33:243–248.

54 Patko D, *et al.* 2024. Smart soils track the formation of pH gradients across the rhizosphere. *Plant Soil*. 500:91–104.

55 Ge S, Dupuy LX, MacDonald MP. 2021. In situ laser manipulation of root tissues in transparent soil. *Plant Soil*. 468:475–489.

56 Ge S, *et al.* 2023. In situ control of root–bacteria interactions using optical trapping in transparent soil. *J Exp Bot*. 74:787–799.

57 Fernández A, *et al.* 2024. Simultaneous two- and three-photon deep imaging of autofluorescence in bacterial communities. *Sensors*. 24:667.

58 Kuo CT. *Customized porosity in ceramic composites via freeze casting*. California Institute of Technology, 2021.

59 Enke TN, *et al.* 2019. Modular assembly of polysaccharide-degrading marine microbial communities. *Curr Biol*. 29: 1528–1535.e6.

60 Daims H, Brühl A, Amann R, Schleifer K-H, Wagner M. 1999. The domain-specific probe EUB338 is insufficient for the detection of all *Bacteria*: development and evaluation of a more comprehensive probe set. *Syst Appl Microbiol.* 22:434–444.

61 CRC Handbook of Chemistry and Physics. 83rd Edition Edited by David R. Lide (National Institute of Standards and Technology). CRC Press: Boca Raton. 2002. + 2664 pp. $139.95. ISBN 0-8493-0483-0. *J Am Chem Soc*. 124:14280.